Inorganic Chemistry

Article

Slicing the Perovskite Structure with Crystallographic Shear Planes: The $A_nB_nO_{3n-2}$ Homologous Series

Artem M. Abakumov,*,[†,‡] Joke Hadermann,[†] Maria Batuk,[†] Hans D'Hondt,[†] Oleg A. Tyablikov,[‡] Marina G. Rozova,[‡] Konstantin V. Pokholok,[‡] Dmitry S. Filimonov,[‡] Denis V. Sheptyakov,[§] Alexander A. Tsirlin,[∥] Daniel Niermann,[⊥] Joachim Hemberger,[⊥] Gustaaf Van Tendeloo,[†] and Evgeny V. Antipov[‡]

[†]*Electron Microscopy for Materials Research (EMAT), University of Antwerp, Groenenborgerlaan 171, B-2020, Antwerp, Belgium,* [‡]*Department of Chemistry, Moscow State University, 119991 Moscow, Russia,* [§]*Laboratory for Neutron Scattering, ETH Zurich and Paul Scherrer Institut (PSI), CH-5232 Villigen, Switzerland,* [∥]*Max Planck Institute for Chemical Physics of Solids, Nöthnitzer Str. 40, 01187 Dresden, Germany, and* [⊥]*Institute of Physics II, University of Cologne, Zülpicher Str. 77, 50937 Cologne, Germany*

A new $A_nB_nO_{3n-2}$ homologous series of anion-deficient perovskites has been evidenced by preparation of the members with $n = 5$ ($Pb_{2.9}Ba_{2.1}Fe_4TiO_{13}$) and $n = 6$ ($Pb_{3.8}Bi_{0.2}Ba_2Fe_{4.2}Ti_{1.8}O_{16}$) in a single phase form. The crystal structures of these compounds were determined using a combination of transmission electron microscopy and X-ray and neutron powder diffraction (S.G. *Ammm*, $a = 5.74313(7)$, $b = 3.98402(4)$, $c = 26.8378(4)$ Å, $R_I = 0.035$, $R_P = 0.042$ for $Pb_{2.9}Ba_{2.1}Fe_4TiO_{13}$ and S.G. *Imma*, $a = 5.7199(1)$, $b = 3.97066(7)$, $c = 32.5245(8)$ Å, $R_I = 0.032$, $R_P = 0.037$ for $Pb_{3.8}Bi_{0.2}Ba_2Fe_{4.2}Ti_{1.8}O_{16}$). The crystal structures of the $A_nB_nO_{3n-2}$ homologues are formed by slicing the perovskite structure with $(\bar{1}01)_p$ crystallographic shear (CS) planes. The shear planes remove a layer of oxygen atoms and displace the perovskite blocks with respect to each other by the $1/2[110]_p$ vector. The CS planes introduce edge-sharing connections of the transition metal−oxygen polyhedra at the interface between the perovskite blocks. This results in intrinsically frustrated magnetic couplings between the perovskite blocks due to a competition of the exchange interactions between the edge- and the corner-sharing metal−oxygen polyhedra. Despite the magnetic frustration, neutron powder diffraction and Mössbauer spectroscopy reveal that $Pb_{2.9}Ba_{2.1}Fe_4TiO_{13}$ and $Pb_{3.8}Bi_{0.2}Ba_2Fe_{4.2}Ti_{1.8}O_{16}$ are antiferromagnetically ordered below $T_N = 407$ and 343 K, respectively. The $Pb_{2.9}Ba_{2.1}Fe_4TiO_{13}$ and $Pb_{3.8}Bi_{0.2}Ba_2Fe_{4.2}Ti_{1.8}O_{16}$ compounds are in a paraelectric state in the 5−300 K temperature range.

Introduction

The flexibility of the ABO_3 perovskite structure and its ability to accommodate cationic or anionic vacancies and a wide range of cations with different oxidation states lead to a variety of perovskite-based compounds with versatile physical properties. The magnetic and electric properties of perovskites arise from a complex interplay between the crystal structure and the electronic state of the transition metal. An extra parameter controlling the magnetic and electric transport properties of perovskites is the dimensionality of the metal−oxygen network. The parent three-dimensional (3D) framework of corner-sharing BO_6 octahedra can be split into quasi two-dimensional (2D) perovskite blocks by an insertion or a subtraction of atomic layers. The perovskite blocks are virtually infinite in two dimensions and have a variable thickness along the stacking axis. By changing the thickness of the perovskite blocks, one arrives at a homologous series of perovskite-type compounds.

The majority of the perovskite-based homologous series are anion-excessive. In the $A_{n+1}B_nO_{3n+1}$ Ruddlesden−Popper series, $A_nB_nO_{3n+1}$ Dion-Jacobson series, and $Bi_2A_{n-1}B_nO_{3n+3}$ Aurivillius series, the O/B ratio exceeds three, because extra oxygen or metal−oxygen layers are added between the $\{001\}_p$-shaped perovskite blocks.[1−7] Another anion-excessive homologous series, $A_nB_nO_{3n+2}$, is based on $\{110\}_p$-shaped perovskite blocks separated by extra oxygen layers.[8,9] Numerous homologous series are also known in complex layered cuprates, where

*To whom correspondence should be addressed. Phone: +32 3 265 32 59. Fax: +32 3 265 32 57. E-mail: artem.abakumov@ua.ac.be.

(1) Ruddlesden, S. N.; Popper, P. *Acta Crystallogr.* **1957**, *10*, 538–539.
(2) Ruddlesden, S. N.; Popper, P. *Acta Crystallogr.* **1958**, *11*, 54–54.
(3) Dion, M.; Ganne, M.; Tournoux, M. *Mater. Res. Bull.* **1981**, *16*, 1429–1435.
(4) Jacobson, A. J.; Johnson, J. W.; Lewandowski, J. T. *Inorg. Chem.* **1985**, *24*, 3727–3729.
(5) Aurivillius, B. *Ark. Kemi* **1949**, *1*, 463–480.
(6) Aurivillius, B. *Ark. Kemi* **1949**, *1*, 499–512.
(7) Aurivillius, B. *Ark. Kemi* **1950**, *2*, 512–527.
(8) Scheunemann, K.; Müller-Buschbaum, H. *J. Inorg. Nuclear Chem.* **1974**, *36*, 1965–1970.
(9) Levin, I.; Bendersky, L. A. *Acta Crystallogr., Sect. B* **1999**, *55*, 853–866.

the perovskite modules form ordered intergrowths with slabs of the rock salt and/or fluorite type structures.[10,11] A layered ordered arrangement of oxygen vacancies can also slice the perovskite structure into 2D blocks. If the vacancies are confined to the $(001)_p$ A□ (□, anion vacancy) layers, the neighboring BO_6 octahedra are transformed into BO_5 tetragonal pyramids.[12] Irrespective of the slicing method (the addition or the subtraction of the oxygen atoms), breaking the connections between the BO_6 polyhedra leads to a reduction in the interblock couplings; i.e., the 2D character of the crystal structure induces 2D features of the electronic structure (here, the "coupling" implies electron hopping probabilities that are reduced to exchange integrals for insulators).

In this contribution, we demonstrate that a new homologous series of perovskite-type anion-deficient structures can be generated by the periodic insertion of nonconservative translation interfaces into the perovskite framework.[13,14] Such interfaces are similar to the crystallographic shear planes that reduce the oxygen content in binary oxides. Starting from $Pb_2Ba_2Fe_4O_{10}$ as the simplest structure of this type,[15] we have varied the thickness of the perovskite blocks between the interfaces, thus obtaining two higher members of the novel perovskite-based $A_nB_nO_{3n-2}$ homologous series. A remarkable feature of this structure type is a competition of magnetic interactions at the interface between the perovskite blocks, potentially resulting in frustrated interblock coupling.

Experimental Section

Synthesis and Composition. The samples were synthesized using a high temperature solid state reaction. The starting materials, PbO, $BaCO_3$, Bi_2O_3, Fe_2O_3, and TiO_2, were mixed in 3.1:2:0:2.05:0.9 and 4.0:2.0:0.1:2.1:1.8 molar ratios for the $Pb_{2.9}Ba_{2.1}Fe_4TiO_{13}$ and $Pb_{3.8}Bi_{0.2}Ba_2Fe_{4.2}Ti_{1.8}O_{16}$ samples, respectively. The mixtures were homogenized thoroughly and heated in the air at 750 °C for 20 h and 830 °C for 48 h with intermediate regrinding. For the final treatment, the samples were reground, pressed into pellets, and heated at 1000 °C for 3 h in an Ar flow. The cation composition was confirmed by energy dispersive X-ray (EDX) analysis performed with a JEOL 5510 scanning electron microscope equipped with the Oxford INCA system. The formal oxidation state +3 of the Fe cations was confirmed by [57]Fe Mössbauer spectroscopy.

X-Ray and Neutron Powder Diffraction. Powder X-ray diffraction (PXD) data for phase analysis and cell parameter determination were collected on a Huber G670 Guinier diffractometer (Cu $K_{\alpha 1}$ radiation, curved Ge monochromator, transmission mode, image plate). Powder neutron diffraction (PND) data were collected at the high resolution powder diffractometer HRPT at the Swiss spallation neutron source SINQ, ETH Zurich and Paul Scherrer Institut (PSI), Switzerland (wavelength $\lambda = 1.494$ Å) with the use of a radiation-type furnace at high temperatures up to 550 K. Crystal structure refinement was performed with the JANA2000 program.[16]

Transmission Electron Microscopy. Electron diffraction patterns were obtained on Philips CM20 and FEI Tecnai G^2 transmission electron microscopes. High resolution transmission electron microscopy (HRTEM) images were recorded on a JEOL 4000EX microscope. The HRTEM images were simulated by means of the JEMS software.

[57]Fe Mössbauer spectroscopy. Mössbauer spectroscopy experiments ([57]Fe) were performed in the transmission mode using a constant acceleration Mössbauer spectrometer coupled with a 1024 multichannel analyzer. A [57]Co/Rh γ-ray source, maintained at room temperature, was used for the measurements. The spectrometer was calibrated with standard α-Fe or sodium nitroprusside absorbers. All isomer shift values (δ) are referred to α-Fe. All experimental data were resolved in sets with Lorenzian line shapes using an iterative least-squares fitting.

Evaluation of the Exchange Couplings. Exchange couplings were estimated using density functional theory band structure calculations. The calculations were performed for $Pb_2Ba_2Fe_4O_{10}$, which has the simplest structure within the homologous series.[15] The calculations were performed by the FPLO9 program.[17] To obtain accurate values of total energies, the mean-field correction for correlation effects in the Fe 3d shell was included via the LSDA+U method. Total energies for different magnetic ordering patterns were mapped onto the classical Heisenberg model; thus leading exchange couplings were derived. Further details of the computational procedure are given in the Supporting Information.

Dielectric Characterization. The dielectric permittivity measurements were carried out employing a pseudo-four-probe geometry and a frequency response analyzer with a high-impedance interface (Novocontrol) for electric field stimulation on the order of 1 V/mm and in a frequency range between 1 Hz and 1 MHz. The disk-like samples had a diameter of typically $D \approx$ 5 mm with a thickness of $d \approx 1$ mm and were cooled down in a commercial [4]He magneto-cryostat (Oxford) in the temperature range 5 K < T < 300 K and in magnetic fields up to 5 T. For the characterization of the nonlinear response, a high-voltage amplifier-module (Novocotrol) was utilized in a two-probe geometry and in the kHz-frequency regime.

Results

Preliminary Characterization. The PXD data revealed that the $Pb_{2.9}Ba_{2.1}Fe_4TiO_{13}$ and $Pb_{3.8}Bi_{0.2}Ba_2Fe_{4.2}Ti_{1.8}O_{16}$ samples are single phase and contain compounds with a perovskite-type structure only. The PXD patterns were indexed in an orthorhombic unit cell with lattice parameters $a = 5.74313(7)$, $b = 3.98402(4)$, and $c = 28.8378(4)$ Å for $Pb_{2.9}Ba_{2.1}Fe_4TiO_{13}$ and $a = 5.7199(1)$, $b = 3.97066(7)$, and $c = 32.5245(8)$ Å for $Pb_{3.8}Bi_{0.2}Ba_2Fe_{4.2}Ti_{1.8}O_{16}$. A comparison to the PXD pattern of $Pb_2Ba_2Fe_4O_{10}$ revealed that the intensity and the splittings of the subcell reflections are very similar for all three compounds[15] and that the only essential difference is in the positions of the supercell reflections due to the significantly different c parameter. Since the $Pb_2Ba_2Fe_4O_{10}$ structure can be interpreted as a sequence of quasi-2D perovskite blocks stacked along the c axis, one can attribute the difference in the c parameter to a different thickness of the perovskite block, i.e., to the formation of the homologous series. The lattice parameters of $Pb_2Ba_2Fe_4O_{10}$, $Pb_{2.9}Ba_{2.1}Fe_4TiO_{13}$, and $Pb_{3.8}Bi_{0.2}Ba_2Fe_{4.2}Ti_{1.8}O_{16}$ are related to the parameter of the parent perovskite structure a_p as $a \approx a_p\sqrt{2}$, $b \approx a_p$, and $c \approx 9.7$ Å + $(n-2)a_p\sqrt{2}$. In the c parameter, the first term of the sum represents the thickness of the interface between the perovskite blocks (nearly

(10) Antipov, E. V.; Abakumov, A. M. *Phys. Uspekhi* **2008**, *51*, 180–190.
(11) Abakumov, A. M.; Shpanchenko, R. V.; Antipov, E. V.; Kovba, L. M.; Kopnin, E. M.; Putilin, S. N. *Russ. Chem. Rev.* **1995**, *64*, 719–729.
(12) Anderson, M. T.; Vaughey, J. T.; Poeppelmeier, K. R. *Chem. Mater.* **1993**, *5*, 151–165.
(13) Abakumov, A. M.; Hadermann, J.; Van Tendeloo, G.; Antipov, E. V. *J. Am. Ceram. Soc.* **2008**, *91*, 1807–1813.
(14) Abakumov, A. M.; Hadermann, J.; Bals, S.; Nikolaev, I. V.; Antipov, E. V.; Van Tendeloo, G. *Angew. Chem., Int. Ed.* **2006**, *45*, 6697–6700.
(15) Nikolaev, I. V.; D'Hondt, H.; Abakumov, A. M.; Hadermann, J.; Balagurov, A. M.; Bobrikov, I. A.; Sheptyakov, D. V.; Pomjakushin, V.Yu.; Pokholok, K. V.; Filimonov, D. S.; Van Tendeloo, G.; Antipov, E. V. *Phys. Rev. B* **2008**, *78*, 024426.
(16) Petricek, V.; Dusek, M. *The crystallographic computing system JANA2000*; Institute of physics: Praha, Czech Republic, 2000.

(17) Koepernik, K.; Eschrig, H. *Phys. Rev. B* **1999**, *59*, 1743.

constant for all compounds), while the second term stands for the thickness of the perovskite block itself. n is the homologue number, and $a_p \approx 4.06$ Å. Thus, $Pb_2Ba_2Fe_4O_{10}$, $Pb_{2.9}Ba_{2.1}Fe_4TiO_{13}$, and $Pb_{3.8}Bi_{0.2}Ba_2Fe_{4.2}Ti_{1.8}O_{16}$ can be considered as members $n = 4$, 5, and 6 of a new $A_nB_nO_{3n-2}$ (A = Pb, Bi, Ba, B = Fe, Ti) homologous series, respectively.

Structure Solution and Refinement. The crystal structure determination was performed using room temperature PXD data. The *Ammm* and *Imma* space groups, as determined by electron diffraction (see below), and the $Pb_{2.9(1)}Ba_{2.14(9)}Fe_{4.0(1)}Ti_{1.0(1)}$ and $Pb_{3.7(1)}Bi_{0.16(6)}$-$Ba_{2.16(8)}Fe_{4.1(1)}Ti_{1.9(1)}$ cation compositions, as determined with the EDX analysis, were used as input for the starting models of $Pb_{2.9}Ba_{2.1}Fe_4TiO_{13}$ and $Pb_{3.8}Bi_{0.2}Ba_2Fe_{4.2}$-$Ti_{1.8}O_{16}$. According to Mössbauer spectroscopy, the formal iron oxidation state is +3; thus no anion deficiency is present with respect to the $A_5B_5O_{13}$ and $A_6B_6O_{16}$ formulas. Starting atomic coordinates for the anion and cation positions were derived from the $A_4B_4O_{10}$ ($n = 4$) structure assuming an expanded thickness of the perovskite block by one and two octahedral layers for the $n = 5$ and $n = 6$ members, respectively. After the refinement of the atomic coordinates and the Pb/Ba occupancy factors for the A positions, low reliability factors were achieved ($R_I = 0.028$ and $R_P = 0.068$ for $Pb_{2.9}Ba_{2.1}Fe_4TiO_{13}$ and $R_I = 0.044$ and $R_P = 0.082$ for $Pb_{3.8}Bi_{0.2}Ba_2Fe_{4.2}Ti_{1.8}$-$O_{16}$). This indicates the correctness of the structure models. Fine details of the crystal structures were determined using PND.

PND revealed that both $Pb_{2.9}Ba_{2.1}Fe_4TiO_{13}$ and $Pb_{3.8}$-$Bi_{0.2}Ba_2Fe_{4.2}Ti_{1.8}O_{16}$ are in an antiferromagnetically (AFM) ordered state at room temperature. The PND experiments for the structure refinement were performed at $T = 550$ K, above the Neel temperature for both compounds ($T_N = 407 \pm 6$ K and 343 ± 14 K for $Pb_{2.9}Ba_{2.1}$-Fe_4TiO_{13} and $Pb_{3.8}Bi_{0.2}Ba_2Fe_{4.2}Ti_{1.8}O_{16}$, respectively; the temperature evolution of the intensity of the magnetic reflections is provided in Figure S1 of the Supporting Information). Because of the large difference between the scattering lengths of Ti and Fe (Ti, -0.344; Fe, 0.945) as well as Pb and Ba (Pb, 0.9405; Ba, 0.507), accurate occupancies of the B and A positions can be obtained. The refinement of the anisotropic atomic displacement parameter for the O(4) atom revealed a large U_{11} component, and this atom was displaced along the a axis from the 4-fold to 8-fold position with halved occupancy. The final refinement was performed with an isotropic approximation for the atomic displacement parameters. The PND profile fittings are presented in Figure 1. The crystallographic data are listed in Table 1. The atomic coordinates are listed in Tables 2 and 3 for $Pb_{2.9}Ba_{2.1}Fe_4TiO_{13}$ and $Pb_{3.8}Bi_{0.2}Ba_2Fe_{4.2}Ti_{1.8}O_{16}$, respectively. The main interatomic distances are presented in Table 4 for $Pb_{2.9}Ba_{2.1}Fe_4TiO_{13}$ and in Table 5 for $Pb_{3.8}$-$Bi_{0.2}Ba_2Fe_{4.2}Ti_{1.8}O_{16}$.

The crystal structures of $Pb_{2.9}Ba_{2.1}Fe_4TiO_{13}$ and $Pb_{3.8}$-$Bi_{0.2}Ba_2Fe_{4.2}Ti_{1.8}O_{16}$ consist of a framework of BO_6 and BO_5 polyhedra (Figure 2a). The corner-sharing BO_6 octahedra form quasi-2D perovskite blocks shaped by $(\bar{1}01)_p$ perovskite lattice planes. The blocks are connected to each other through chains of edge-sharing BO_5 distorted tetragonal pyramids. The chains can adopt two mirror-related configurations ("left" (L) and "right" (R)). The chains differ by opposite directions of the sideways
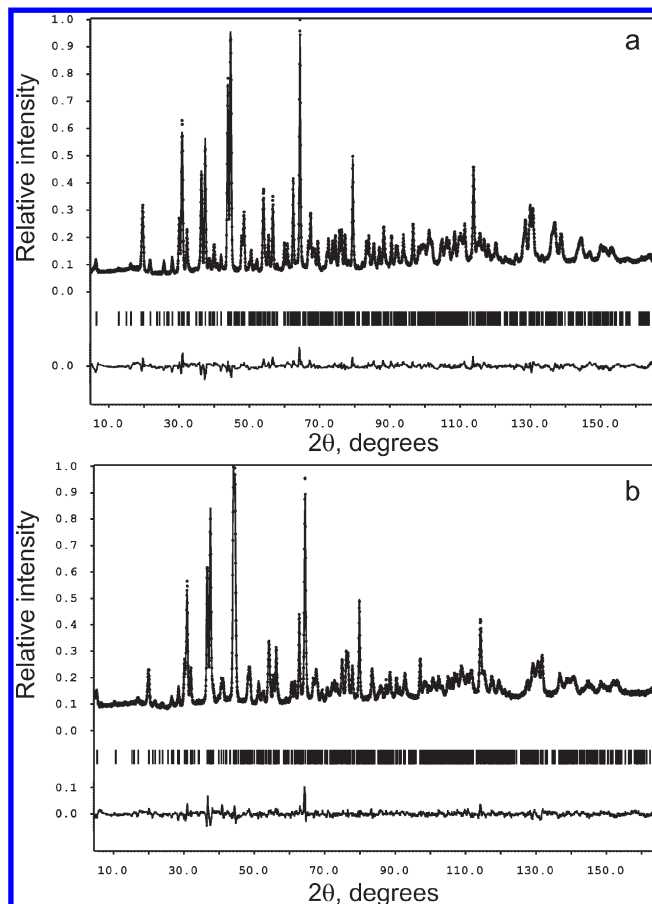

Figure 1. Experimental, calculated, and difference neutron powder diffraction profiles for $Pb_{2.9}Ba_{2.1}Fe_4TiO_{13}$ (a) and $Pb_{3.8}Bi_{0.2}Ba_2Fe_{4.2}$-$Ti_{1.8}O_{16}$ (b) at $T = 550$ K.

Table 1. Selected Parameters from Rietveld Refinement for $Pb_{2.9}Ba_{2.1}Fe_4TiO_{13}$ and $Pb_{3.8}Bi_{0.2}Ba_2Fe_{4.2}Ti_{1.8}O_{16}$

formula	$Pb_{2.9}Ba_{2.1}Fe_4TiO_{13}$	$Pb_{3.8}Bi_{0.2}Ba_2Fe_{4.2}$-$Ti_{1.8}O_{16}$
space group	*Ammm*	*Imma*
a, Å	5.7687(2)	5.7439(3)
b, Å	4.0048(1)	3.9888(2)
c, Å	26.9236(8)	32.633(2)
Z	2	2
cell volume, Å³	622.00(4)	747.68(9)
calcd density, g/cm³	7.305	7.462
T, K	550	550
radiation	neutron, $\lambda = 1.494$ Å	neutron, $\lambda = 1.494$ Å
2θ range, step, deg.	$5 \leq 2\theta \leq 165$; 0.05	$5 \leq 2\theta \leq 165$; 0.05
params refined	23	27
R_I, R_P, R_{wP}	0.035, 0.042, 0.053	0.032, 0.037, 0.048

displacement of the O(4) oxygen atoms at the common edge of the tetragonal pyramids. The random arrangement of the R and L chains causes splitting of the O(4) oxygen position into two positions with 50% occupancy (Figure 2b). The tetragonal pyramidal chains are connected to the BO_6 octahedra of the perovskite block through common corners, together delimiting six-sided tunnels filled with double chains of the A cations with a lone electron pair (Pb^{2+}, Bi^{3+}). In both the $Pb_{2.9}Ba_{2.1}Fe_4$-TiO_{13} and $Pb_{3.8}Bi_{0.2}Ba_2Fe_{4.2}Ti_{1.8}O_{16}$ structures, the cation positions in the BO_5 tetragonal pyramids are occupied exclusively by the Fe^{3+} cations. The distribution of the Fe^{3+} and Ti^{4+} cations among the octahedral

Table 2. Positional and Atomic Displacement Parameters for $Pb_{2.9}Ba_{2.1}Fe_4TiO_{13}$ at $T = 550$ K

atom	site	occupancy	x/a	y/b	z/c	U_{iso}, Å^2
Pb1	4j	1	1/2	1/2	0.3056(2)	0.032(1)
BaPb1	4i	0.7Ba+0.3Pb	0	0	0.0996(3)	0.041(2)
BaPb2	2d	0.7Ba+0.3Pb	1/2	1/2	1/2	0.028(2)
Fe1	4i	1	0	0	0.2935(2)	0.026(1)
FeTi1	4j	0.72Fe+0.28Ti	1/2	0	0.3970(2)	0.011(1)
FeTi2	2b	0.56Fe+0.44Ti	0	0	1/2	0.014(2)
O1	4j	1	1/2	1/2	0.3904(2)	0.032(1)
O2	8n	1	0.239(1)	0	0.4453(2)	0.028(1)
O3	8n	1	0.2572(8)	0	0.3368(1)	0.027(1)
O4	8n	0.5	0.0401(9)	0	0.2195(2)	0.018(1)
O5	2a	1	0	1/2	1/2	0.020(2)

Table 3. Positional and Atomic Displacement Parameters $Pb_{3.8}Bi_{0.2}Ba_2Fe_{4.2}Ti_{1.8}O_{16}$ at $T = 550$ K

atom	site	occupancy	x/a	y/b	z/c	U_{iso}, Å^2
Pb1	4e	1	0	3/4	0.4558(2)	0.044(2)
BaPb1	4e	0.5Ba+0.5Pb	1/2	3/4	0.3708(3)	0.045(2)
BaPb2	4e	0.5Ba+0.5Pb	1/2	3/4	0.2069(3)	0.042(2)
Fe1	4e	1	1/2	1/4	0.4644(2)	0.047(2)
FeTi1	4e	0.6Fe+0.4Ti	1/2	1/4	0.1222(3)	0.009(2)
FeTi2	4e	0.5Fe+0.5Ti	1/2	3/4	0.7071(6)	0.011(2)
O1	4e	1	1/2	3/4	0.1135(3)	0.044(3)
O2	8i	1	0.752(1)	3/4	0.6612(2)	0.035(2)
O3	8i	1	0.239(1)	1/4	0.4277(2)	0.034(1)
O4	8i	0.5	0.547(2)	3/4	0.4736(3)	0.027(2)
O5	4e	1	1/2	1/4	0.7064(3)	0.020(1)
O6	4d	1	3/4	3/4	3/4	0.037(2)

Table 4. Selected Interatomic Distances for $Pb_{2.9}Ba_{2.1}Fe_4TiO_{13}$ (Å) at $T = 550$ K

Pb1−O1	2.284(7) × 1	Fe1−O3	1.883(5) × 2
Pb1−O3	2.585(3) × 4	Fe1−O4	2.005(7) × 1
Pb1−O4	2.739(5) × 1	Fe1−O4	2.046(1) × 2
BaPb1−O1	2.8969(9) × 2	FeTi1−O1	2.0101(7) × 2
BaPb1−O2	2.715(4) × 4	FeTi1−O2	1.992(7) × 2
BaPb1−O3	3.025(5) × 4	FeTi1−O3	2.144(6) × 2
BaPb1−O5	2.682(7) × 1		
		FeTi2−O2	2.016(6) × 4
BaPb2−O1	2.951(6) × 2	FeTi2−O5	2.0023(1) × 2
BaPb2−O2	2.907(2) × 8		
BaPb2−O5	2.8843(1) × 2		

Table 5. Selected Interatomic Distances for $Pb_{3.8}Bi_{0.2}Ba_2Fe_{4.2}Ti_{1.8}O_{16}$ (Å) at $T = 550$ K

Pb1−O1	2.26(1) × 1	Fe1−O3	1.919(8) × 2
Pb1−O3	2.590(5) × 4	Fe1−O4	2.04(1) × 1
Pb1−O4	2.67(1) × 1	Fe1−O4	2.035(1) × 2
BaPb1−O1	2.917(2) × 2	FeTi1−O1	2.014(2) × 2
BaPb1−O2	2.678(6) × 4	FeTi1−O2	1.91(1) × 2
BaPb1−O3	3.109(7) × 4	FeTi1−O3	2.13(1) × 2
BaPb1−O5	2.52(1) × 1		
		FeTi2−O2	2.08(2) × 2
BaPb2−O1	3.05(1) × 1	FeTi2−O5	1.9946(3) × 2
BaPb2−O2	2.868(7) × 4	FeTi2−O6	2.01(1) × 2
BaPb2−O5	2.8720(1) × 2		
BaPb2−O5	2.83(1) × 1		
BaPb2−O6	2.832(5) × 4		

Figure 2. Crystal structures of the $n = 4-6$ members of the $A_nB_nO_{3n-2}$ homologous series of anion-deficient perovskites. (a) 3D view of $Pb_2Ba_2Fe_4O_{10}$ ($n = 4$) (after [15]), $Pb_{2.9}Ba_{2.1}Fe_4TiO_{13}$ ($n = 5$), and $Pb_{3.8}Bi_{0.2}Ba_2Fe_{4.2}Ti_{1.8}O_{16}$ ($n = 6$). Yellow distorted tetragonal pyramids are occupied exclusively by the Fe cations. The Pb cations in the six-sided tunnels are shown as orange spheres (Pb, Bi for $n = 6$). The blue octahedra are centered either by Fe cations ($n = 4$) or jointly by Fe and Ti cations ($n = 5, 6$). The Pb and Ba atoms in the perovskite blocks are shown as large blue spheres. Oxygen atoms are shown as small blue spheres. Perovskite blocks are marked by brackets. (b) Two mirror-related configurations of the double chains of FeO_5 tetragonal pyramids occurring in the structures in a disordered manner.

Figure 3. Local coordination environment of transition metal and Pb cations. (a) Fe and Ti cations in the $Pb_{2.9}Ba_{2.1}Fe_4TiO_{13}$ structure. (b) Fe and Ti cations in the $Pb_{3.8}Bi_{0.2}Ba_2Fe_{4.2}Ti_{1.8}O_{16}$ structure. (c) Pb cations in the six-sided tunnels of the $Pb_{2.9}Ba_{2.1}Fe_4TiO_{13}$ structure. Only one configuration (marked as R in Figure 2b) of the $Fe(1)O_5$ tetragonal pyramidal chain is shown for clarity.

and tetragonal pyramidal sites is also supported by Mössbauer spectroscopy (see below). We find that the 5- and 6-fold coordinated Fe^{3+} cations are present in a ~50:50 ratio in both compounds, which implies that all Ti^{4+} cations are located in the octahedra of the perovskite blocks. The Fe^{3+} and Ti^{4+} cations are intermixed at the octahedral sites, but their distribution is not completely random: the octahedra at the periphery of the perovskite block (the FeTi(1) position) contain more Fe than the octahedra in the interior part of the perovskite block (the
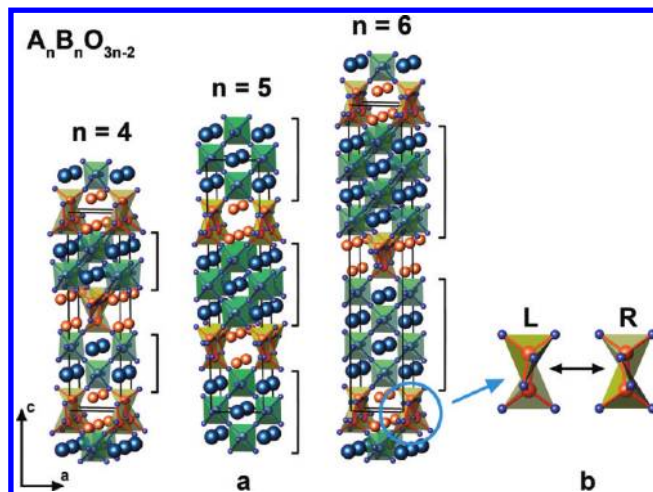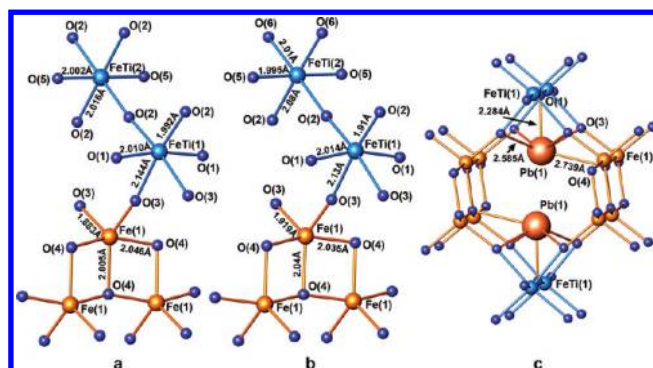
FeTi(2) position). This distribution is in agreement with the local electroneutrality rule, which requires an increasing amount of the B^{4+} cations on going toward the center of the perovskite block. The FeTi(2) octahedra are only slightly deformed, whereas the octahedral environment of the FeTi(1) cations is strongly distorted due to a displacement of the FeTi(1) cations from the O(3)−O(3) edge toward the O(2)−O(2) edge (d(FeTi(1)) − O(3) = 2.13− 2.14 Å; d(FeTi(1)) − O(2) = 1.91 − 1.99 Å; Figure 3a,b). This displacement is caused by an electrostatic repulsion due to close FeTi(1)−Pb(1) contact. The Pb cations in the six-sided tunnels between the perovskite blocks are 6-fold coordinated. Their coordination environment is very asymmetric with a shortest Pb−O distance of 2.26−2.28 Å and a longest distance of 2.67−2.74 Å (Figure 3c). The open coordination polyhedron of the Pb
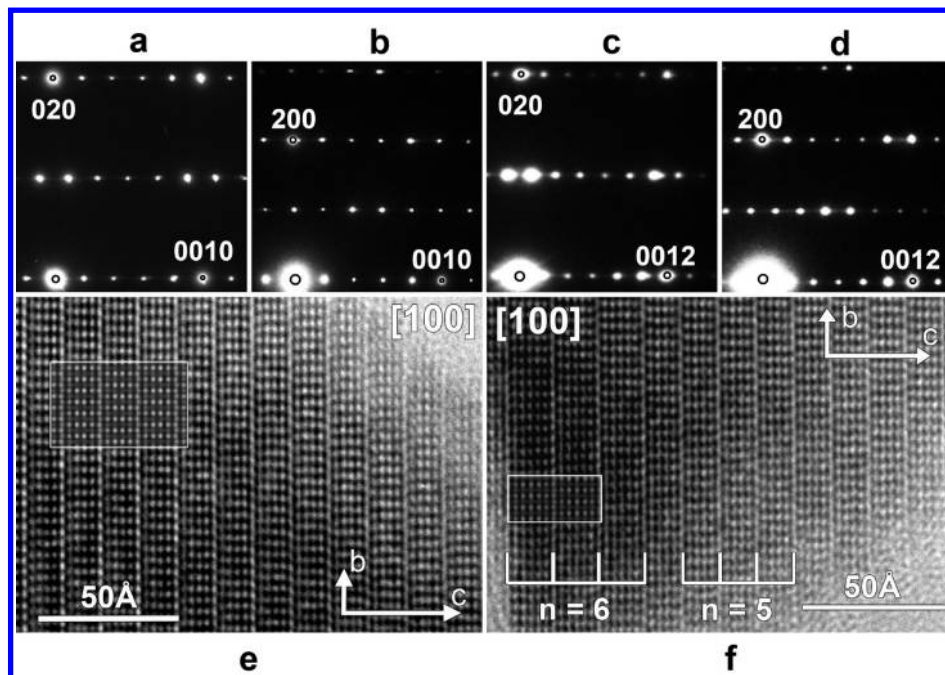
Figure 4. Electron diffraction (ED) patterns and high resolution transmission electron microscopy (HRTEM) images for the $n = 5$ and $n = 6$ members. (a, b) ED patterns for $Pb_{2.9}Ba_{2.1}Fe_4TiO_{13}$ along the [100] (a) and [010] (b) directions. (c, d) ED patterns for $Pb_{3.8}Bi_{0.2}Ba_2Fe_{4.2}Ti_{1.8}O_{16}$ along the [100] (c) and [010] (d) directions. (e) [100] HRTEM image of the $n = 5$ structure. The calculated image (focus value $f = -250$ Å, crystal thickness $t = 57$ Å) is inserted (outlined with a white rectangle). (f) [100] HRTEM image of the intergrowth of the $n = 5$ and $n = 6$ structures. The calculated image for the $n = 6$ structure ($f = -250$ Å, $t = 52$ Å) is inserted (outlined with a white rectangle).

cations is completed by a localized electron pair. The lone pair domains are directed toward the center of the six-sided tunnel as we have previously demonstrated by analyzing the electron localization function for $Pb_2Ba_2Fe_4O_{10}$ ($n = 4$).[15]

Transmission Electron Microscopy. The well-ordered stacking of the perovskite blocks is evident from the electron diffraction patterns of $Pb_{2.9}Ba_{2.1}Fe_4TiO_{13}$ and $Pb_{3.8}Bi_{0.2}Ba_2Fe_{4.2}Ti_{1.8}O_{16}$ (Figure 4a–d). The electron diffraction patterns of both compounds can be completely indexed on the basis of the orthorhombic unit cell determined from PXD data. The brightest reflection along the $00l$ reciprocal lattice rows corresponding to an interplanar spacing of $d \approx 2.7$ Å is a perovskite subcell reflection and can be indexed as $0\ 0\ 2n$, where n is the homologue number. Sharp reflections and the absence of diffuse intensity lines along the c^* axis evidence the low amount of stacking faults. The extinction conditions determined from a complete reconstruction of reciprocal space are in agreement with the space groups $Ammm$ and $Imma$ for $Pb_{2.9}Ba_{2.1}Fe_4TiO_{13}$ and $Pb_{3.8}Bi_{0.2}Ba_2Fe_{4.2}Ti_{1.8}O_{16}$, respectively.

High resolution transmission electron microscopy images reveal the long-range ordered sequence of perovskite blocks with uniform thickness (Figure 4e, Figure S2 of the Supporting Information). Planar defects, commonly observed in perovskite-based homologous series, are occasionally found: they show up as single lamellae of the $n + 1$ member in the matrix of the n member (Figure S3 of the Supporting Information) or as intergrowths of domains of the $n + 1$ and n members (Figure 4f). The refined structures were supported by comparing the calculated and experimental [100] HRTEM images. The calculated images of the $n = 5$ structure (focus value $f = -250$ Å, crystal thickness $t = 57$ Å)

and the $n = 6$ structure ($f = -250$ Å, $t = 52$ Å) are in excellent agreement with the experiment.

^{57}Fe Mössbauer Spectroscopy. The Mössbauer spectra of $Pb_{2.9}Ba_{2.1}Fe_4TiO_{13}$ and $Pb_{3.8}Bi_{0.2}Ba_2Fe_{4.2}Ti_{1.8}O_{16}$ in the paramagnetic region are shown in Figure 5a,b. For both compounds, the spectra were fitted with two doublets, designated as $A1_1$ and $B1_1$ for $Pb_{2.9}Ba_{2.1}Fe_4TiO_{13}$ and $A2_1$ and $B2_1$ for $Pb_{3.8}Bi_{0.2}Ba_2Fe_{4.2}Ti_{1.8}O_{16}$, of nearly equal area (parameters are listed in Table S1 of the Supporting Information). The observed isomer shifts, $IS = 0.28$–0.31 mm/s, correspond to Fe^{3+} cations exclusively.[18] According to their IS values, the "A" doublets are attributed to the octahedral crystallographic positions and the "B" doublets to the 5-fold coordinated ones.[15] The observed ratios of the "A" to "B" doublet areas are 0.96(4):1.04(4) for $Pb_{2.9}Ba_{2.1}Fe_4TiO_{13}$ and 1.08(4):0.92(4) for $Pb_{3.8}Bi_{0.2}Ba_2Fe_{4.2}Ti_{1.8}O_{16}$, in a very good agreement with the relative amounts of Fe^{3+} in the octahedral and tetragonal pyramidal coordination for both compounds (1.00:1.00 for $Pb_{2.9}Ba_{2.1}Fe_4TiO_{13}$ and 1.05:0.95 for $Pb_{3.8}Bi_{0.2}Ba_2Fe_{4.2}Ti_{1.8}O_{16}$, see Tables 2 and 3).

Mössbauer spectra of $Pb_{2.9}Ba_{2.1}Fe_4TiO_{13}$ and $Pb_{3.8}Bi_{0.2}Ba_2Fe_{4.2}Ti_{1.8}O_{16}$ measured below the Néel temperatures are shown in Figure 5c,d. The transitions from the paramagnetic to AFM state for both compounds are extended over a wide temperature range of ~ 100 K, where the paramagnetic doublets are observed along with the magnetic sextets. The spectra for both compounds are composed of two sets of Zeeman sextets with different hyperfine parameters, designated as $A1_n$ and $B1_n$ for $Pb_{2.9}Ba_{2.1}Fe_4TiO_{13}$ and $A2_n$ and $B2_n$ for $Pb_{3.8}Bi_{0.2}Ba_2Fe_{4.2}Ti_{1.8}O_{16}$. The "A" groups of sextets with $IS = 0.47$–0.52 mm/s, negative values of apparent quadrupole shifts, ε's, and

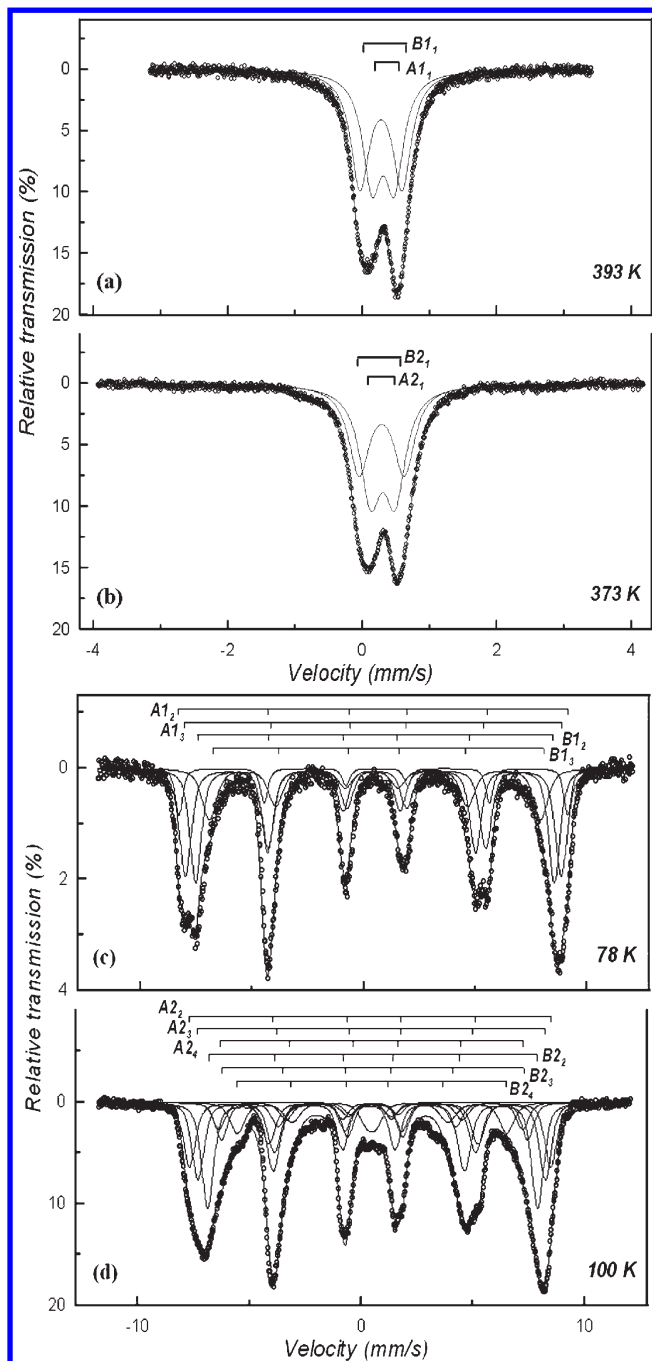(18) Menil, F. *J. Phys. Chem. Solids* **1985**, *46*, 763.

Figure 5. ^{57}Fe Mössbauer spectra of $Pb_{2.9}Ba_{2.1}Fe_4TiO_{13}$ (a, c) and $Pb_{3.8}Bi_{0.2}Ba_2Fe_{4.2}Ti_{1.8}O_{16}$ (b, d) measured above (a, b) and below (c, d) the transition temperature to the AFM ordered state.

generally higher values of magnetic hyperfine fields, H_{hf}'s, are attributed to the octahedrally coordinated FeTi(1) and FeTi(2) sites. The "B" sextets, which are characterized by smaller values of IS = 0.43–0.46 mm/s and H_{hf}'s, and positive ε values, correspond to 5-fold coordinated Fe(1) sites (Table S1 of Supporting Information).

   Band Structure Calculations and Evaluation of the Exchange Couplings. The LDA band structure of $Pb_2Ba_2Fe_4O_{10}$ (Figure S7 of the Supporting Information) shows Fe 3d states at the Fermi level (zero energy), O 2p states

below −2 eV, and Pb 6s states at −8 eV, in agreement with the previously reported band structures of Pb-containing transition metal oxides.[19] The 6s shell of Pb is nearly filled and confirms the oxidation state of +2 for the Pb atoms. The LDA energy spectrum is gapless, since LDA does not account for correlation effects in the Fe 3d shell. The application of LSDA+U/GGA+U leads to an insulating spectrum with a band gap of about 1.5 eV at U = 5 eV (Figure S8 of the Supporting Information). Such a band gap is in reasonable agreement with the brown color of the compound. Magnetic moments on both Fe sites amount to 4.5 μ_B and are slightly below the spin-only value of 5 μ_B. Strong AFM couplings were found between the Fe^{3+} species (spin of 5/2) with exchange integrals J of 80–120 K within the perovskite blocks. The coupling between the edge-sharing tetragonal pyramids (Fe−O−Fe angle close to 90°) is ferromagnetic (FM) and amounts to $J_1 \sim −8$ K. The coupling between the corner-sharing pyramids (Fe−O−Fe angle close to 180°) is AFM with $J_2 \sim 90$ K.

   Dielectric Properties. In order to evaluate possible ferroelectric or even magneto-dielectric contributions, an analysis of the dielectric response was performed for both $Pb_{2.9}Ba_{2.1}Fe_4TiO_{13}$ and $Pb_{3.8}Bi_{0.2}Ba_2Fe_{4.2}Ti_{1.8}O_{16}$ within the AFM ordered state (5 K < T < 300 K). Figure 6 displays the temperature-dependent complex permittivity $\varepsilon^*(T)$ for frequencies between 1 Hz and 1 MHz together with the related two-point conductivity $\sigma' = \omega\varepsilon_0\varepsilon''$ for $Pb_{3.8}Bi_{0.2}Ba_2Fe_{4.2}Ti_{1.8}O_{16}$ ($Pb_{2.9}Ba_{2.1}Fe_4TiO_{13}$ shows similar behavior, see the Supporting Information, Figures S4, S5). The real part of the dielectric permittivity $\varepsilon'(T)$ decreases monotonously in two significant steps from a high value (∼10 000) at room temperature to lower values at 5 K (Figure 6a). These features are strongly frequency-dependent: the steps shift to higher T with increasing stimulation frequency and are accompanied by corresponding peak-like structures in the dielectric loss $\varepsilon''(T)$ (Figure 6b) which are superimposed to a frequency-dependent background. The latter is related to thermally activated conductivity (see Figure 6c), which gives a contribution $\varepsilon'' \sim \sigma'/\omega$. This type of behavior can be explained due to the heterogeneous character of the samples. The interfaces separating the perovskite blocks give rise to additional resistive contributions and have to be considered for the interpretation of the dielectric measurements. The high permittivity values are contributions from highly capacitive depletion layers formed at the "intrinsic" sample interfaces as well as between the sample material and electrodes.[20] These interface capacities together with the resistance of the interface form an effective RC element in series with the intrinsic resistivity. Thus, the intrinsic resistivity is enhanced (i.e., conductivity is reduced), and a large capacitive contribution is added for low enough frequencies. The underlying time constant τ = RC is strongly temperature-dependent due to the thermally activated semiconducting characteristic of R. For high enough frequencies and at low enough temperatures, this effective RC contribution is cut short and the bulk properties prevail. At low temperatures, ε' is frequency-independent and has a value of about 20 for $Pb_{2.9}Ba_{2.1}Fe_4TiO_{13}$ and 115 for $Pb_{3.8}Bi_{0.2}Ba_2Fe_{4.2}Ti_{1.8}O_{16}$. The latter value is clearly enhanced compared to other transition metal oxides. Nevertheless, such a high

   (19) Tsirlin, A. A.; Belik, A. A.; Shpanchenko, R. V.; Antipov, E. V.; Takayama-Muromachi, E.; Rosner, H. *Phys. Rev. B* **2008**, *77*, 092402.

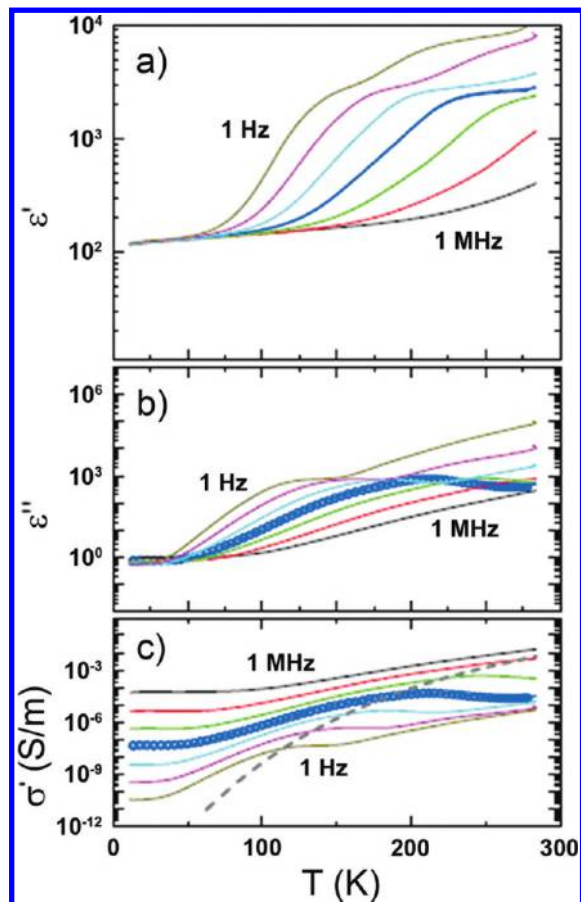   (20) Lunkenheimer, P.; et al. *Phys. Rev. B* **2002**, *66*, 052105.

Figure 6. Temperature dependence of the complex dielectric permittivity (a, b) and conductivity (c) for $Pb_{3.8}Bi_{0.2}Ba_2Fe_{4.2}Ti_{1.8}O_{16}$. The data were measured for frequencies between 1 Hz and 1 MHz (logarithmically spaced by a factor of 10) with a stimulus of $\sim$1 V/mm in zero magnetic field (solid lines). For 1 kHz, the data measured in a magnetic field of 5T are also displayed ($\bigcirc$) revealing no significant differences from the zero field results. The dashed line in the conductivity plot is drawn to guide the eyes onto the estimation of the residual bulk DC conductivity.

value of ε' alone is not indicative of ferroelectricity. Looking at the 1 MHz data (Figure 6a), no anomaly can be detected which could result from a polar ordering (at least up to 300 K). The estimated intrinsic conductivity is displayed as a dashed line in Figure 6c and shows a thermally activated behavior. At low temperatures (and higher frequencies), the conductivity is enhanced by hopping processes, typical for such disordered semiconductors.[20] Neither dielectric nor conductivity contributions are altered by the appliance of a magnetic field of 5 T as demonstrated for the 1 kHz curves in Figure 6.

In order to further elucidate the dielectric ground state of the materials, we performed permittivity measurements in electric fields up to $E = 250$ V/mm at the temperatures 10 K and 160 K, as displayed in Figure 7. At 160 K, where the interface contributions are present, a significant electric field dependence of ε^* can be detected. Most notably, with increasing E, the dielectric loss $\varepsilon'' \sim \sigma'/\omega$ is increased. But no hysteresis effects can be found in the $\varepsilon''(E)$ curve. Such behavior can be explained by (Schottky-)diode-like nonlinear characteristics and does not point toward ferroelectricity. Correspondingly, these nonlinearities are absent at low temperatures, while for a ferroelectric ground state, some E-field dependence could
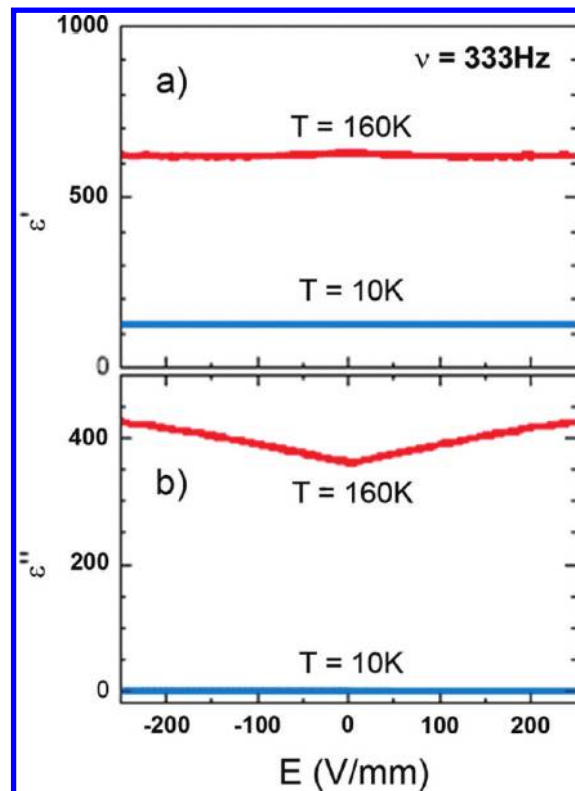

Figure 7. Electric-field dependence of the complex permittivity for $Pb_{3.8}Bi_{0.2}Ba_2Fe_{4.2}Ti_{1.8}O_{16}$.

be expected (full temperature dependence of the dielectric nonlinearities can be found in the Supporting Information, Figure S6). Thus, we conclude that both compounds are paraelectric below the AFM transition. It should be mentioned that near T_N the conductivity of the samples is too high to study the possible onset of spontaneous dielectric polarization directly by appropriate pyro-current experiments.

Discussion

The existence of the new anion-deficient $A_nB_nO_{3n-2}$ homologous series is demonstrated by the preparation of two successive members with $n = 5$ and $n = 6$. Considering the $Pb_2Ba_2Fe_4O_{10}$ compound as the $n = 4$ member of this series, we increased the oxygen content and the thickness of the perovskite blocks between the interfaces by the partial replacement of Fe^{3+} with a B cation that has a formal charge of $+4$ and a strong affinity toward octahedral coordination, being Ti^{4+}. The cation compositions and synthesis conditions were then adjusted in order to obtain macroscopically pure phases and to avoid disordered intergrowths and intermixing of different homologues. The $A_nB_nO_{3n-2}$ structures can be represented as a sequence of atomic layers stacked along the $[10\bar{1}]_p$ direction of the perovskite subcell (Figure 8c), see Chart 1. The oxygen

Chart 1

$$-ABO-(O_2-ABO)_{n-2}-O_2-ABO-ABO-(O_2-ABO)_{n-2}-O_2-ABO-$$
$$\underset{c}{\longleftarrow}$$

layers are missing at the interfaces between two perovskite blocks, resulting in anion deficiency and the
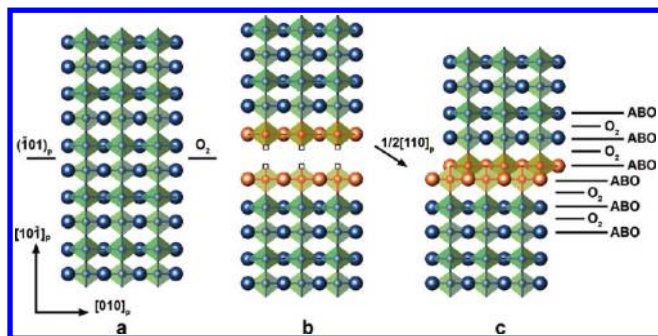
Figure 8. Interface between two perovskite blocks in the $A_nB_nO_{3n-2}$ homologous series. (a) Initial perovskite matrix; the $(\bar{1}01)_p$ interface plane passes through the oxygen layer. (b) Cut of the perovskite matrix along the interface plane; the oxygen atoms to be removed are marked with squares. (c) Closing the gap by a displacement of the top part over the $1/2[110]_p$ vector resulting in the interface with the missing oxygen layer.

$A_nB_nO_{3n-2}$ composition. A fragmentation of the structure into quasi-2D blocks by periodically spaced nonconservative (i.e., changing the chemical composition) interfaces implies the subtraction of one or more atomic layers and the closing of the gap by displacing one part of the structure with respect to the other by a vector which is a fraction of a lattice translation of the parent structure. A displacement component normal to the subtracted atomic layer must be present for a nonconservative interface, resulting in a compositional change. In the $A_nB_nO_{3n-2}$ homologous series, such nonconservative translational interfaces can formally be described as the result of slicing the perovskite structure along the $(\bar{1}01)_p$ lattice plane (Figure 8a), subtracting the oxygen layer (Figure 8 b), and subsequently displacing the upper part of the structure by the $1/2[110]_p$ vector (Figure 8c). The displacement introduces edge sharing for the metal–oxygen polyhedra along the interface instead of the corner sharing in the parent perovskite structure. This operation is a crystallographic shear operation and the translation interface is a crystallographic shear (CS) plane.[21] The $A_nB_nO_{3n-2}$ homologous series therefore results from a fragmentation of the perovskite structure by periodically spaced $1/2[110](\bar{1}01)_p$ CS planes (the first term indicates the displacement vector and the second term indicates the indexes of the interface plane in the perovskite subcell). The crystallographic derivation of such CS planes is similar to that of the CS planes in the ReO_3-type structure, which is based on a perovskite framework with completely vacant A positions. Similar to the $A_nB_nO_{3n-2}$ homologues, the thickness of the ReO_3-type block between the CS planes can be varied, resulting in the homologous series M_nO_{3n-1} ($1/2[10\bar{1}](102)$ CS planes), M_nO_{3n-2} ($1/2[10\bar{1}](103)$ CS planes) (M = Mo, W), where n is the number of MO_6 octahedra between two successive parallel CS planes.[22,23]

The electronic coupling between the perovskite blocks is fundamentally different in the $A_nB_nO_{3n-2}$ compounds, compared to other perovskite-based homologous series. The B–O–B connections between the perovskite blocks are typically interrupted by an interleave with electronically inactive slabs, such as the (A_2O_2) rock-salt-type slabs in the
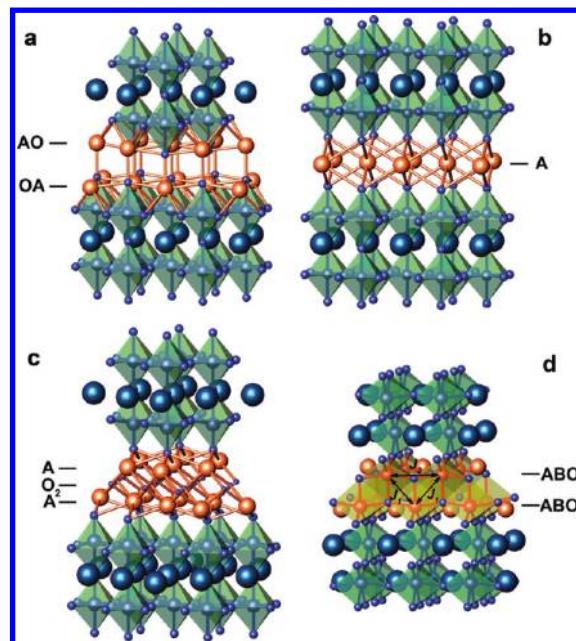

Figure 9. Interfaces between the perovskite blocks in the perovskite-based homologous series. (a) The $A_{n+1}B_nO_{3n+1}$ Ruddlesden–Popper series with the rock-salt-type AO–OA slab. (b) The $A_nB_nO_{3n+1}$ Dion–Jacobson series with the A-cation layer between the perovskite blocks. (c) The $Bi_2A_{n-1}B_nO_{3n+3}$ Aurivillius series with the α-PbO-type Bi–O_2–Bi slab. (d) The $A_nB_nO_{3n-2}$ series with two successive ABO layers; J_1 and J_2 are the competing B–O–B couplings along the chain of the BO_5 tetragonal pyramids. The structures are viewed nearly along the $\langle 110 \rangle$ direction of the perovskite subcell.

$A_{n+1}B_nO_{3n+1}$ Ruddlesden–Popper compounds,[1,2] single A-cation layers in the $A_nB_nO_{3n+1}$ Dion–Jacobson compounds,[3,4] or (Bi_2O_2) slabs with in the $Bi_2A_{n-1}B_nO_{3n+3}$ Aurivillius compounds (Figure 9a–c).[5–7] Therefore, the interlayer couplings are orders of magnitude below the intralayer couplings. This, however, does not preclude the conventional AFM ordering along the stacking axis (two perovskite blocks in the magnetic unit cell).

We have proposed a different strategy to achieve a perovskite-based homologous series. Crystallographic shear planes create 2D perovskite blocks, but the B cations of the neighboring blocks remain sufficiently close to each other and reveal a sizable coupling, J_1, that amounts to 10% of the intralayer couplings. Despite this sizable coupling, the magnetic ordering can be impeded due to the intrinsic frustration of the interactions J_1 and J_2 (Figure 9d). If the spins follow J_1 and align ferromagnetically, the AFM interaction J_2 is disfavored. Yet the AFM order induced by J_2 is unfavorable for the FM J_1. The resulting magnetic structure is not obvious. Indeed, we have observed an unusual AFM ordering with four perovskite blocks in the magnetic unit cell of $Pb_2Ba_2Fe_4O_{10}$.[15] The frustrated spin–lattice of the $A_nB_nO_{3n-2}$ homologues is somewhat reminiscent of the exotic magnetic behavior in $BaCuSi_2O_6$, where the reduced dimensionality manifests itself in the unconventional regime of the Bose–Einstein condensation.[24] We expect the intrinsic magnetic frustration to drive a range of unusual physical properties in the $A_nB_nO_{3n-2}$ homologues with various transition-metal B cations.

(21) Van Landuyt, J.; De Ridder, R.; Gevers, R.; Amelinckx, S. *Mater. Res. Bull.* **1970**, *5*, 353–362.
(22) Magneli, A. *Acta Chem. Scand.* **1948**, *2*, 501–517.
(23) Gado, P.; Magneli, A. *Acta Chem. Scand.* **1965**, *19*, 1514–1515.

(24) Sebastian, S. E.; Harrison, N.; Batista, C. D.; Balicas, L.; Jaime, M.; Sharma, P. A.; Kawashima, N.; Fisher, I. R. *Nature* **2006**, *441*, 617–620.

The $Pb_{2.9}Ba_{2.1}Fe_4TiO_{13}$ and $Pb_{3.8}Bi_{0.2}Ba_2Fe_{4.2}Ti_{1.8}O_{16}$ compounds are the obvious analogues of the magnetoelectric perovskites containing both d^n (in this case, Fe^{3+}) and d^0 (in this case, Ti^{4+}) cations in the B sublattice. In such magneto-electric perovskites as $Pb(Fe_{2/3}W_{1/3})O_3$, the diamagnetic d^0 cations are responsible for ferroelectricity, whereas the magnetic ordering is achieved due to the magnetically active d^n cations.[25,26] The ferroelectric displacements are additionally driven by the lone pair Pb^{2+} cations.[27,28] However, $Pb_{2.9}Ba_{2.1}Fe_4TiO_{13}$ and $Pb_{3.8}Bi_{0.2}Ba_2Fe_{4.2}Ti_{1.8}O_{16}$ remain paraelectric down to 5 K, even in spite of a relatively high concentration of the d^0 cation in the perovskite blocks ($\sim$50% in $Pb_{3.8}Bi_{0.2}Ba_2Fe_{4.2}Ti_{1.8}O_{16}$). We can suggest that either the interfaces between the perovskite blocks serve as effective barriers for cooperative ferroelectric displacements or the concentration of the lone pair cations at the A positions of the perovskite blocks is insufficient to promote such displacements. The dielectric behavior of the $A_nB_nO_{3n-2}$ homologues should be more extensively investigated as a function of the thickness of the perovskite block, d^0, and lone pair cation concentration. This work is now underway.

Conclusions

We have demonstrated that the perovskite structure can be sliced with an ordered array of crystallographic shear planes. The thickness of the perovskite block between the shear planes is readily varied, leading to the $A_nB_nO_{3n-2}$ homolo-gous series of anion-deficient perovskite-type compounds. The existence of this new homologous series of anion-deficient perovskites is proven by the preparation of the compounds with n up to 6 as single phases. A general feature of the new homologous series is the frustrated nature of the interactions between individual perovskite blocks. Such interactions can lead to a wide range of physical properties for doped systems or isostructural compounds with other transition metals. Referring to the long and rich history of research on perovskites, especially layered compounds,[29] we expect the $A_nB_nO_{3n-2}$ homologues to be a playground for preparing new materials as well as for studying fundamental physical phenomena in strongly correlated electronic systems.

(25) Smolenskii, G. A.; Agranovskaya, A. I.; Isupov, V. A. *Sov. Phys. Sol. Stat.* **1959**, *1*, 907–909.
(26) Bokov, V. A.; Mylnikova, I. E.; Smolenskii, G. A. *Sov. Phys. JETP* **1962**, *15*, 447–449.
(27) Khomskii, D. I. *J. Magn. Magn. Mater.* **2006**, *306*, 1–8.
(28) Baettig, P.; Spaldin, N. A. *Appl. Phys. Lett.* **2005**, *86*, 012505.
(29) Raveau, B. *Prog. Solid State Chem.* **2007**, *35*, 171–173.